

Nonlinear dynamics of a classical rotating pendulum systemwith multiple excitations

Ning Han(韩宁), Pei-Pei Lu(鲁佩佩)

Citation: Chin. Phys. B . 2020, 29(11): 110502 . **doi:** 10.1088/1674-1056/ab9df2
Journal homepage: http://cpb.iphy.ac.cn; http://iopscience.iop.org/cpb

What follows is a list of articles you may be interested in

Chaotic signal denoising algorithm based on sparse decomposition

Jin-Wang Huang(黄锦旺), Shan-Xiang Lv(吕善翔), Zu-Sheng Zhang(张足生), Hua-Qiang Yuan(袁华强)

Chin. Phys. B . 2020, 29(6): 060505 . **doi:** 10.1088/1674-1056/ab8a3b

Hidden attractors in a new fractional-order discrete system: Chaos, complexity, entropy, and control

Adel Ouannas, Amina Aicha Khennaoui, Shaher Momani, Viet-Thanh Pham, Reyad El-Khazali

Chin. Phys. B . 2020, 29(5): 050504 . **doi:** 10.1088/1674-1056/ab820d

Nonlinear continuous bi-inductance electrical line with dissipative elements: Dynamics of the low frequency modulated waves

S M Ngounou, F B Pelap

Chin. Phys. B . 2020, 29(4): 040502 . **doi:** 10.1088/1674-1056/ab75d6

Homoclinic and heteroclinic chaos in nonlinear systems driven by trichotomous noise

You-Ming Lei(雷佑铭), Hong-Xia Zhang(张红霞)

Chin. Phys. B . 2017, 26(3): 030502 . **doi:** 10.1088/1674-1056/26/3/030502

Markov transition probability-based network from time series for characterizing experimental two-phase flow

Gao Zhong-Ke, Hu Li-Dan, Jin Ning-De

Chin. Phys. B . 2013, 22(5): 050507 . **doi:** 10.1088/1674-1056/22/5/050507

Nonlinear dynamics of a classical rotating pendulum system with multiple excitations*

Ning Han(韩宁)† and Pei-Pei Lu(鲁佩佩)

Key Laboratory of Machine Learning and Computational Intelligence, College of Mathematics and Information Science, Hebei University, Baoding 071002, *China*

(Received 6 April 2020; revised manuscript received 9 June 2020; accepted manuscript online 18 June 2020)

We report an attempt to reveal the nonlinear dynamic behavior of a classical rotating pendulum system subjected to combined excitations of constant force and periodic excitation. The unperturbed system characterized by strong irrational nonlinearity bears significant similarities to the coupling of a simple pendulum and a smooth and discontinuous (SD) oscillator, especially the phase trajectory with coexistence of Duffing-type and pendulum-type homoclinic orbits. In order to learn the effect of constant force on this pendulum system, all types of phase portraits are displayed by means of the Hamiltonian function with large constant excitation especially the transitions of complex singular closed orbits. Under sufficiently small perturbations of the viscous damping and constant excitation, the Melnikov method is used to analyze the global structure of the phase space and the feature of trajectories. It is shown, both theoretically and numerically, that this system undergoes a homoclinic bifurcation and then bifurcates a unique attracting rotating limit cycle. Finally, the estimation of the chaotic threshold of the rotating pendulum system with multiple excitations is calculated and the predicted periodic and chaotic motions can be shown by applying numerical simulations.

Keywords: rotating pendulum, Melnikov method, rotating limit cycle, chaotic dynamics

PACS: 05.45.–a, 05.45.Ac, 05.45.Pq **DOI:** 10.1088/1674-1056/ab9df2

1. Introduction

As the earliest forms of physical instrument to describe nonlinearity, pendulums have played a powerful role in promoting the rise of nonlinear science.[1] Ever since Galileo theorized the isochronism of simple pendulums in the 16th century,[2] much attention has been paid to the problems in pendulum systems in the past four centuries. Through considering pendulum dynamics, with and without external forcing, researchers are naturally drawn to essential ideas of linearity and nonlinearity. Throughout the history of pendulum research, a variety of classical pendulum models or systems containing pendulums have been extensively developed so far, such as simple pendulums,[3] inverted pendulums,[4] double pendulums,[5,6] spring pendulums,[7,8] and parametric pendulums.[9–11] Additionally, an explosion of pendulum studies has produced a flood of information on nonlinear dynamics in term of oscillations,[12,13] rotations,[14,15] bifurcations,[16,17] chaos,[18,19] synchronization,[20,21] experimental investigation,[22,23] and energy absorption,[24–26] etc. From the perspectives of historical background, theoretical exploration and engineering application, pendulums are one of the typical and popular nonlinear oscillators that possess complicated and rich dynamical behavior.

It is well known that the Melnikov method is an easy and effective analytic method to study chaotic dynamics[27] in one-dimensional nonlinear systems with small time-periodic perturbation. The analytical solution of homoclinic orbits plays an important role in detecting lower bound lines for Horseshoes chaos. However, it is found that the analytic expression of a homoclinic orbit cannot be obtained for most nonlinear dynamical systems especially the system containing an irrational term. Even if the analytical solution can be derived by means of Hamiltonian, it will also be difficult to compute the generalized Melnikov integrals containing the analytic expression. Therefore, it is very necessary to detect dynamical behavior for complex irrational nonlinear systems by means of the numerical Melnikov method.

A rotating pendulum linked by an oblique spring with a fixed end was presented in Ref. [28], which has shown abundant dynamic behaviors compared with the classical simple pendulum, especially the bistable dynamics and non-smooth characteristics. This pendulum system possesses an irrational and fractional restoring force with trigonometric function, so that the solution of homoclinic orbits cannot be solved analytically. Then the chaotic dynamics for this pendulum system subjected to the viscous damping and periodic excitation is analyzed by means of an approximate analytic method, as seen in Ref. [29]. Additionally, the global bifurcations and different types of limit cycles of this rotating pendulum system with a periodic perturbation have been studied in Ref. [30], including Hopf bifurcation, the homoclinic orbit bifurcation and the saddle-node bifurcation of periodic solution, the oscillat-

*Project supported by the National Natural Science Foundation of China (Grant Nos. 11702078 and 11771115), the Natural Science Foundation of Hebei Province, China (Grant No. A2018201227) and the High-Level Talent Introduction Project of Hebei University, China (Grant No. 801260201111).

†Corresponding author. E-mail: hanning.bing@163.com; ninghan@hbu.edu.cn

© 2020 Chinese Physical Society and IOP Publishing Ltd

ing limit cycle and the rotating limit cycle.

In this paper we try to explore the nonlinear dynamics of a bi-stable pendulum exerted by viscous damping, a constant force and a periodic excitation, which differs from other pendulums. Our bi-stable pendulum can bear double well dynamics owing to influence of coupling of a simple pendulum and a mass-spring oscillator. Herein, the contribution of this paper is to study the effect of a constant excitation on a typical pendulum system characterized by strong irrational nonlinearity. It is found that the constant excitation breaks the symmetry of the system. From a kinematic point of view, our pendulum system possesses both rotational motion and bistable motion, which allow ones to have a better understanding of complex motions in nonlinear dynamical systems. In addition, the results are listed for a better understanding of the rotating limit cycle and different types of chaos in the complicated pendulum system.

This paper is organized as follows. In Section 2, the equation of the rotating pendulum subjected to the viscous damping, constant and periodic excitations can be established. In Section 3, the unperturbed dynamics of the rotating pendulum are investigated using nonlinear dynamical techniques without external perturbation, including nonlinear restoring force, equilibrium bifurcation and phase portrait. In Section 4, the perturbed dynamics are studied by means of the Melnikov method, Bendixson theory and numerical simulations, including the rotating limit cycle, the chaotic thresholds, the periodic and chaotic motions. Section 5 is the conclusion.

2. Equation of motion

Figure 1(a) shows a classical rotating pendulum model, which can be described as a simple pendulum linked by an oblique spring with a fixed end.[28] This rotating pendulum moves in the vertical plane determined by the spring and light rod. Consider the pendulum subjected to a viscous damping of ratio C, a positive constant excitation F_0 and a periodic excitation of amplitude F_1 and frequency Ω in the direction of motion, for which the differential equation can be derived as follows:

$$\begin{aligned} &mLx'' + CLx' + mg\sin x \\ &+ kh\sin x\left(1 - \frac{l}{\sqrt{L^2+h^2-2hL\cos x}}\right) \\ &= F_0 + F_1\cos(\Omega\bar{t}), \end{aligned} \tag{1}$$

where the prime denotes derivative with respect to $\bar{t}$, x is the angular displacement, m represents the lump mass, L denotes the length of massless rod, k and l represent the stiffness and relax length of the linear spring, h is the hight between the rigid supports A and B, always assumed $h > L$. Then, system (1) can be rewritten in the following form:

$$\begin{aligned} &\ddot{x} + \xi\dot{x} + \sin x + q\lambda\sin x\left(1 - \frac{1}{\sqrt{1+\lambda^2-2\lambda\cos x}}\right) \\ &= f_0 + f_1\cos(\omega t), \end{aligned} \tag{2}$$

where

$$t = \sqrt{\frac{g}{L}}\,\bar{t},\quad \xi = \frac{C}{m}\sqrt{\frac{L}{g}},\quad \omega_{\rm p} = \sqrt{\frac{g}{L}},\quad \omega_s = \sqrt{\frac{k}{m}},$$

$$q = \frac{\omega_s^2}{\omega_{\rm p}^2},\ \lambda = \frac{h}{L},\ f_0 = \frac{F_0}{mg},\ f_1 = \frac{F_1}{mg},\ \omega = \sqrt{\frac{L}{g}}\,\Omega,\quad L = l.$$

Notice that one dimensionless parameter q in system (2) mainly reflects the natural frequency ratio of the mass-spring system and the simple pendulum system, and the other dimensionless parameter λ represents the geometric structure of the pendulum model. We always assume that the parameter λ is greater than 1 in the following analysis. From a structural point of view, this rotating pendulum model presented in Fig. 1(a) can be regarded as the coupling of a simple pendulum depicted in Fig. 1(b) and a mass-spring oscillator shown in Fig. 1(c). Interestingly, the mass-spring oscillator bears significant similarities to the SD oscillator,[31,32] which exhibits double well dynamics like the Duffing oscillator.[33–35]

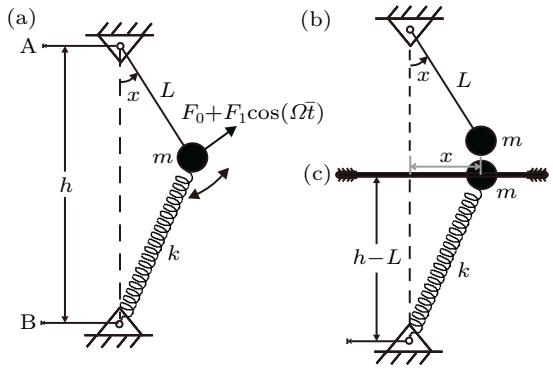


Fig. 1. (a) The physical model of the classical rotating pendulum with multiple excitations, (b) the simple pendulum with rotation feature, (c) the mass-spring oscillator with bi-stable characteristics (SD oscillator).

3. Unperturbed dynamics

The unperturbed dynamics of the rotating pendulum system will be studied directly for the original equation with irrational nonlinearity using nonlinear dynamical techniques, including the nonlinear restoring force, the equilibrium bifurcation set and the phase portrait.

Without considering the external perturbations, for $\xi = 0$, $f_0 = 0$ and $f_1 = 0$, we derive the unperturbed dynamical system of this rotating pendulum as follows:

$$\ddot{x} + \sin x + q\lambda\sin x\left(1 - \frac{1}{\sqrt{1+\lambda^2-2\lambda\cos x}}\right) = 0. \tag{3}$$

Apparently, the nonlinear restoring force can be easily obtained by letting $\ddot{x} = F(x)$,

$$F(x) = -\sin x - q\lambda\sin x\left(1 - \frac{1}{\sqrt{1+\lambda^2-2\lambda\cos x}}\right). \tag{4}$$

Even the stiffness of the spring is linear and the resistance force supplied to the system is strongly irrational nonlinearity due to geometry configuration. Due to its periodicity for $F(x+2\pi)=F(x)$, the dynamical behavior of the unperturbed system (3) can be studied over a period $x\in[-\pi,\pi]$ in the following analysis. Defining $F(x)=0$, the equilibrium positions of the unperturbed system (3) can be easily derived and they are

$$x_1=0,\quad x_2=\pi,\quad x_3=-\pi,\quad x_4=\arccos\rho,$$
$$x_5=-\arccos\rho,\quad \rho=\frac{1+\lambda^2}{2\lambda}-\frac{q^2\lambda}{2(1+q\lambda)^2},\qquad(5)$$

when $|\rho|<1$. The equilibrium bifurcation curve $\mathscr{B}$ in Fig. 2(a) can be plotted by letting $\mathrm{d}F(x)/\mathrm{d}x\,|_{x=0}=0$, and written as

$$\mathscr{B}=\left\{(\lambda,q)\;\middle|\;q=\frac{\lambda-1}{\lambda\,(2-\lambda)},\ \lambda\in(1,2),\ q\in(0,+\infty)\right\},\qquad(6)$$

where

$$\lim_{\lambda\to1^+}q=\lim_{\lambda\to1^+}\frac{\lambda-1}{\lambda\,(2-\lambda)}=0,$$
$$\lim_{\lambda\to2^-}q=\lim_{\lambda\to2^-}\frac{\lambda-1}{\lambda\,(2-\lambda)}=+\infty.$$

Note that the equilibrium bifurcation curve $\mathscr{B}$ divides the parameter space (λ,q) into two regions denoted by I and II respectively. All the possible nonlinear restoring forces of each region are displayed in Figs. 2(b)–2(f), where α and β correspond to two extreme values of $F(x)$ satisfying $F(x_a)=\alpha, F(x_b)=\beta$ and $x_a>x_b$. Interestingly, the nonlinear restoring forces of region II can be divided by the curve $\mathscr{L}$ satisfying $\alpha=\beta$ into two regions denoted by II_1 for $\alpha<\beta$ and II_2 for $\alpha>\beta$, respectively. Clearly, the associated Hamiltonian of system (3) can be given by

$$H(x,y)=\frac{y^2}{2}-(1+q\lambda)\cos x-q\sqrt{1+\lambda^2-2\lambda\cos x}+2q\lambda-q+1,\qquad(7)$$

where $y=\dot{x}$. With the help of Hamiltonian (7), the trajectories of system (3) can be classified by the value of $H(x,y)=e$, for details see Figs. 3(a) and 3(b). For a better understanding of the phase trajectories in system (3), we introduce a symbol Γ_e that can be expressed as

$$\Gamma_e=\begin{cases}\{\,(x,y)\;\mid\;H(x,y)=e,\ e\in[E_0,+\infty),\ (q,\lambda)\in\mathrm{I}\,\},\\ \{\,(x,y)\;\mid\;H(x,y)=e,\ e\in[E_n,+\infty),\ (q,\lambda)\in\mathrm{II}\},\end{cases}$$

where $E_0=H(x_1,0)$, $E_p=H(x_{2,3},0)$ and $E_n=H(x_{4,5},0)$. It is worth pointing out that the energy values E_0, E_p and E_n represent the energy boundaries of different motions from a physical point of view. For example, E_p corresponds to the energy boundary of oscillation ($e<E_p$) and rotation ($e>E_p$). E_0 is the energy boundary of mono-stable oscillation ($e>E_0$) and bi-stable oscillation ($e<E_0$). E_n represents the potential energy of two static equilibria x_4 and x_5.

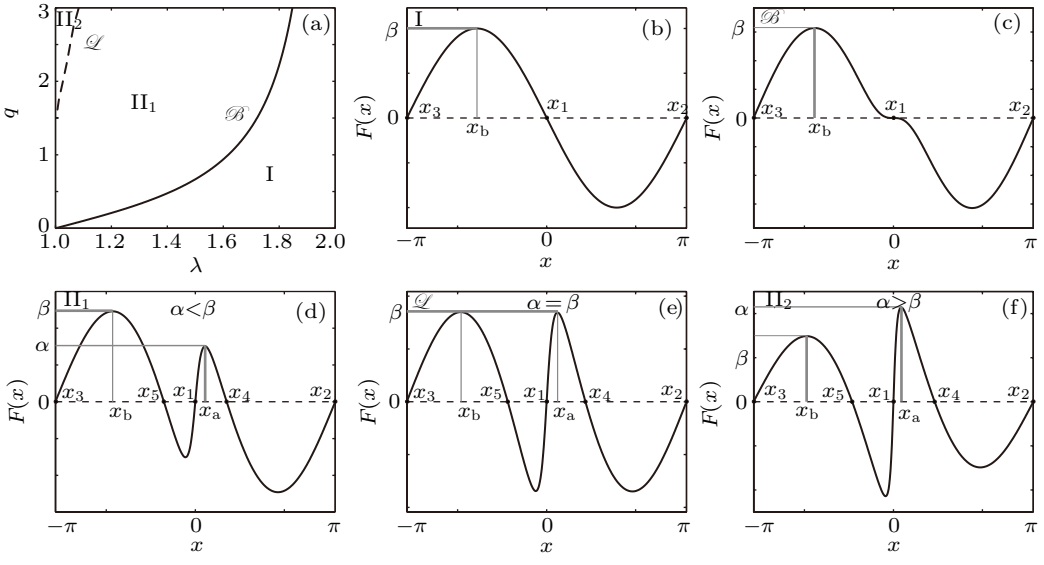


Fig. 2. When $f_0=0$ and $\xi=0$: (a) the equilibrium bifurcation set (λ,q), (b) the nonlinear restoring force for $(\lambda,q)\in\mathrm{I}$, (c) the nonlinear restoring force for $(\lambda,q)\in\mathscr{B}$, (d)–(f) three types of the nonlinear restoring forces for $(\lambda,q)\in\mathrm{II}$, where $\mathrm{II}=\mathrm{II}_1\bigcup\mathscr{L}\bigcup\mathrm{II}_2$.

Take the phase portrait in Fig. 3(b) as an example. The unperturbed system (3) possesses elliptic points $(x_{1,4,5},0)$ and hyperbolic points $(x_{2,3},0)$. When $e\in(E_n,E_0)$, Γ_e represents a pair of left-and-right symmetrical closed orbits colored in green. When e decreases from E_0 to E_n, Γ_e shrinks into the pair of equilibria $(x_4,0)$ and $(x_5,0)$ marked by green solid points. On the other hand, Γ_e extends into the Duffing-type homoclinic orbits (hom1) colored in red when e increases from E_n to E_0. While for $e\in(E_0,E_p)$, Γ_e gives the large closed orbit with blue encircling three equilibria $(x_1,0)$, $(x_4,0)$, $(x_5,0)$ and the

Duffing-type homoclinic orbits. As e increases for $e = E_{\rm p}$, Γ_e extends into the pendulum-type homoclinic orbits (hom2) in red. When $e \in (E_{\rm p}, +\infty)$, Γ_e represents a pair of upper-and-lower symmetrical orbits denoted by black solid lines. The corresponding symbols can be marked in Fig. 3(b).

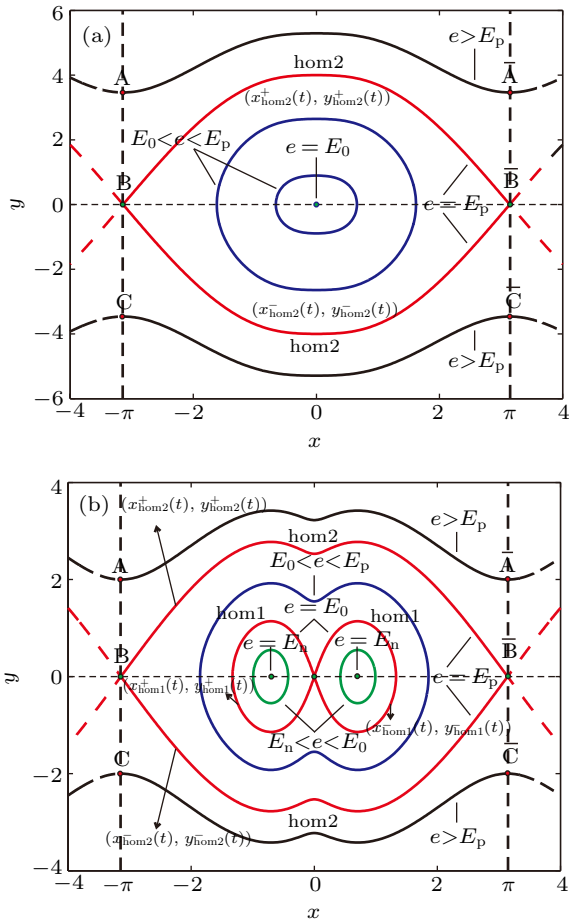


Fig. 3. (a) Phase portrait with the pendulum-type homoclinic orbits for $(\lambda, q) = (2, 3) \in$ I, (b) phase portrait with the coupling of the pendulum-type and Duffing-type homoclinic orbits for $(\lambda, q) = (1.2, 3) \in$ II.

These phase portraits plotted in Figs. 3(a) and 3(b) are, of course, periodic in x with period 2π. In other words, the state of the nonlinear dynamical system is unchanged by the addition of 2π to x. It is an advantage to topologically introduce a cylindrical phase space which allows us to clearly distinguish between the rotational motion and oscillating motion. From a geometric point of view, the cylindrical phase space is obtained by connecting one vertical line $x = -\pi$ (dashed line AC) with the other vertical line $x = \pi$ (dashed line $\overline{A}\,\overline{C}$). Apparently, the cylindrical Hamiltonian can be derived by letting $X = \cos x$, $Y = \sin x$, $Z = \dot{x}$, and written as follows:

$$\begin{cases} H(X,Y,Z) = \dfrac{Z^2}{2} - (1+q\lambda)X \\ \qquad\qquad - q\sqrt{1+\lambda^2-2\lambda X} + 2q\lambda - q + 1, \\ X^2 + Y^2 = 1. \end{cases} \tag{8}$$

Based upon the cylindrical Hamiltonian function (8), two typical cylindrical phase portraits corresponding to Figs. 3(a) and 3(b) are plotted for different values of $H(X,Y,Z) = e$ as shown in Figs. 4(a) and 4(b). It is important to recognize that orbits, e.g., marked by A and $\overline{A}$ in Fig. 3, are in fact closed orbits which encircle the cylinder in Fig. 4: such orbits correspond to rotary rather than oscillatory motions of the pendulum, and two classes of motions are separated by the pendulum-type homoclinic orbits (hom2) to the saddle point. The details of the parameters taken in Fig. 4 can be found in the corresponding captions.

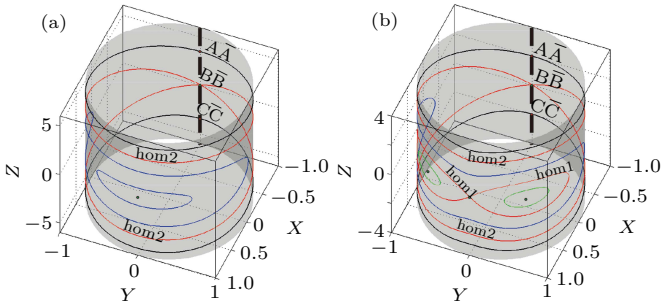


Fig. 4. (a) Cylindrical phase portrait with the pendulum-type homoclinic orbits for $(\lambda, q) = (2, 3) \in$ I, (b) cylindrical phase portrait with the coupling of the pendulum-type and Duffing-type homoclinic orbits for $(\lambda, q) = (1.2, 3) \in$ II.

4. Perturbed dynamics

In this section, the authors will explore the perturbed dynamics of this pendulum system subjected to the viscous damping, constant excitation and periodic excitation using the Melnikov method and numerical simulations.

4.1. The pendulum system with a large constant excitation

In order to learn the effect of constant force[36,37] on this pendulum system, all the possible phase portraits can be analyzed with the help of the Hamiltonian function in this subsection, especially the transitions of singular closed orbits.

When $\xi = 0$ and $f_1 = 0$, the rotating pendulum system (2) is given by

$$\ddot{x} + \sin x + q\lambda \sin x \left(1 - \frac{1}{\sqrt{1+\lambda^2-2\lambda\cos x}}\right) = f_0. \tag{9}$$

Then the nonlinear restoring force of system (9) can be easily obtained as

$$\begin{aligned} F(x, f_0) \;=\; & f_0 - \sin x \\ & - q\lambda \sin x \left(1 - \frac{1}{\sqrt{1+\lambda^2-2\lambda\cos x}}\right). \end{aligned} \tag{10}$$

Letting $F(x, f_0) = 0$, the equilibrium bifurcation diagrams of system (9) for f_0 versus x are shown in Figs. 5(a), 6(a), 7(a), and 8(a), where the dashed lines represent the unstable equilibrium (saddle) and the solid lines denote the stable equilibrium (center). Furthermore, we introduce the notation y for the velocity $\dot{x}$ and obtain the Hamiltonian function with a constant excitation as follows:

$$H(x, y, f_0) \;=\; \frac{y^2}{2} - (1+q\lambda)\cos x - q\sqrt{1+\lambda^2-2\lambda\cos x}$$

$$-f_0x+2q\lambda-q+1. \tag{11}$$

All the types of trajectories of system (9) are plotted for different values of the Hamiltonian function $H(x,y,f_0)=E$, for the details see Figs. 5–8. When $(\lambda,q)\in$ I, the corresponding phase portraits are displayed for different values of parameter f_0 in Fig. 5, where the dashed lines in Figs. 5(b)–5(f) denote the nonlinear restoring forces $F(x,f_0)$. For $f_0=0$, the phase portraits of this pendulum system bear significant similarities to simple pendulum with the pendulum-type homoclinic orbits marked by thick gray lines, as shown in Fig. 5(b). As the constant excitation f_0 grows no more than β, the pendulum-type homoclinic orbits in Fig. 5(b) break and then become the Duffing-type homoclinic orbits marked by the thick gray line in Fig. 5(c). When the constant excitation f_0 continues to increase to β, the Duffing-type homoclinic orbits shrink into an equilibrium (sharp) depicted in Fig. 5(d). Finally, the phase portrait without equilibrium is plotted for $f_0>\beta$ in Fig. 5(e).

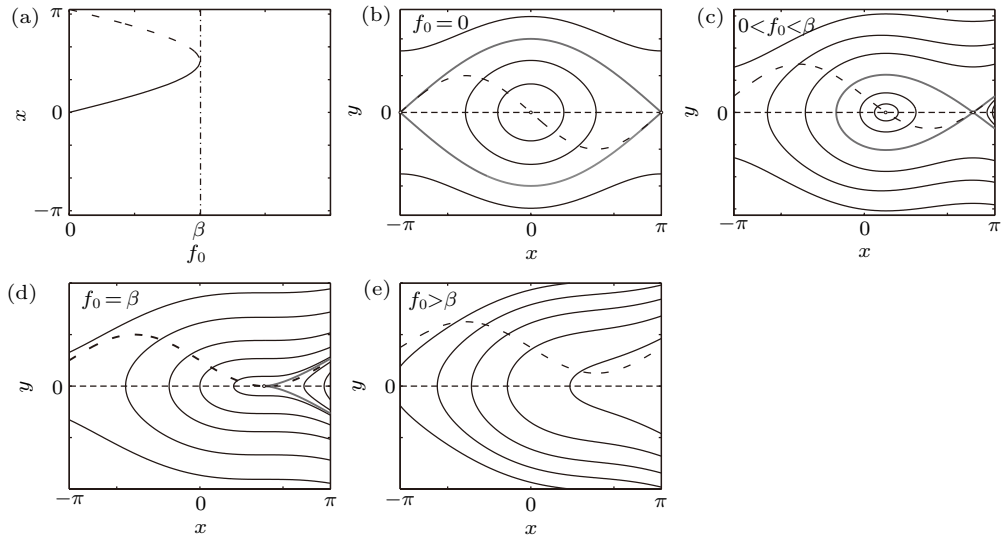


Fig. 5. Dynamic behavior of system (3) for $(\lambda,q)\in$ I: (a) the equilibrium bifurcation diagram for f_0 versus x, (b)–(e) the corresponding phase portraits and the nonlinear restoring forces marked by dashed lines.

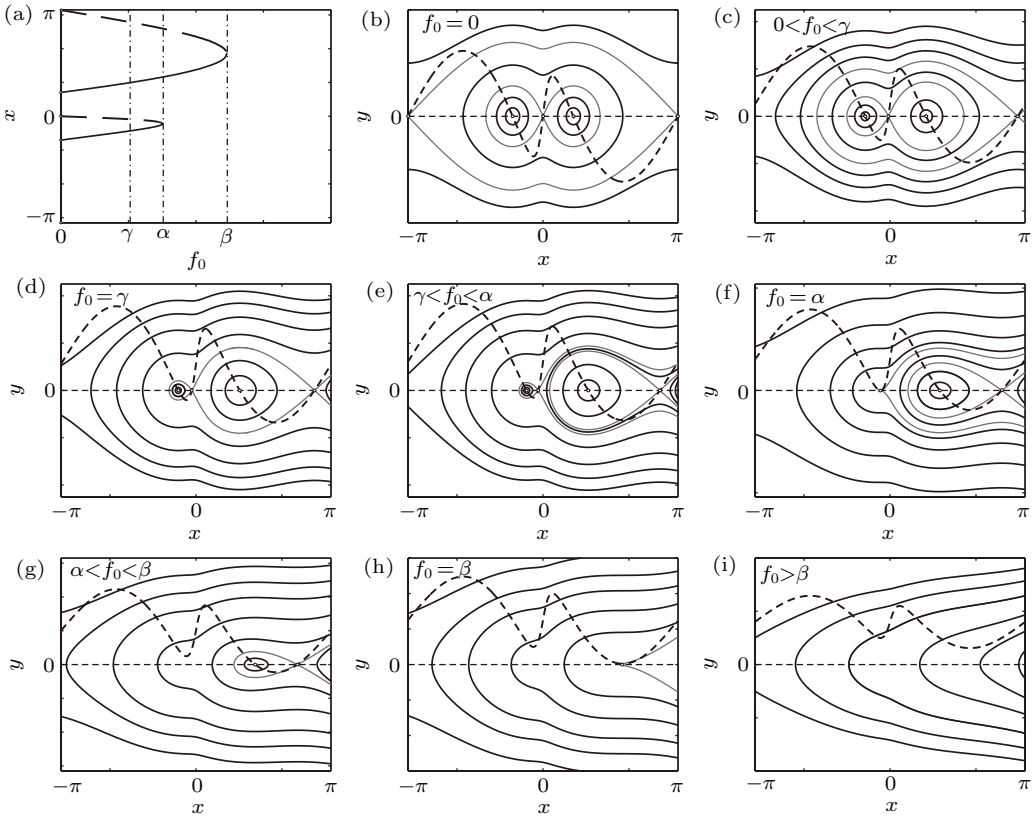


Fig. 6. Dynamic behavior of system (3) for $(\lambda,q)\in$ II$_1$: (a) the equilibrium bifurcation diagram for f_0 versus x, (b)–(i) the corresponding phase portraits and the nonlinear restoring forces marked by dashed lines.

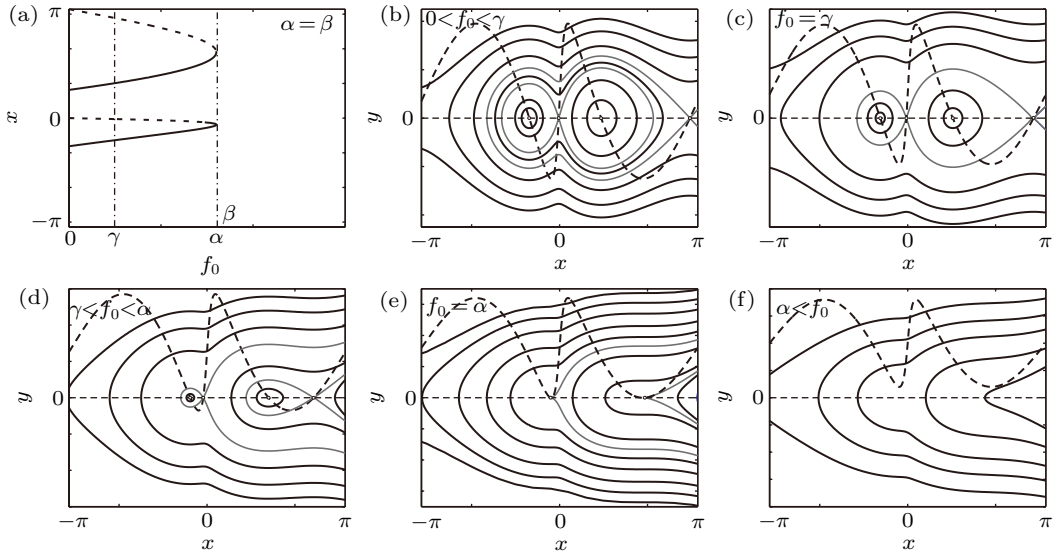


Fig. 7. Dynamic behavior of system (3) for $(\lambda,q)\in\mathscr{L}$: (a) the equilibrium bifurcation diagram for f_0 versus x, (b)–(f) the corresponding phase portraits and the nonlinear restoring forces marked by dashed lines.

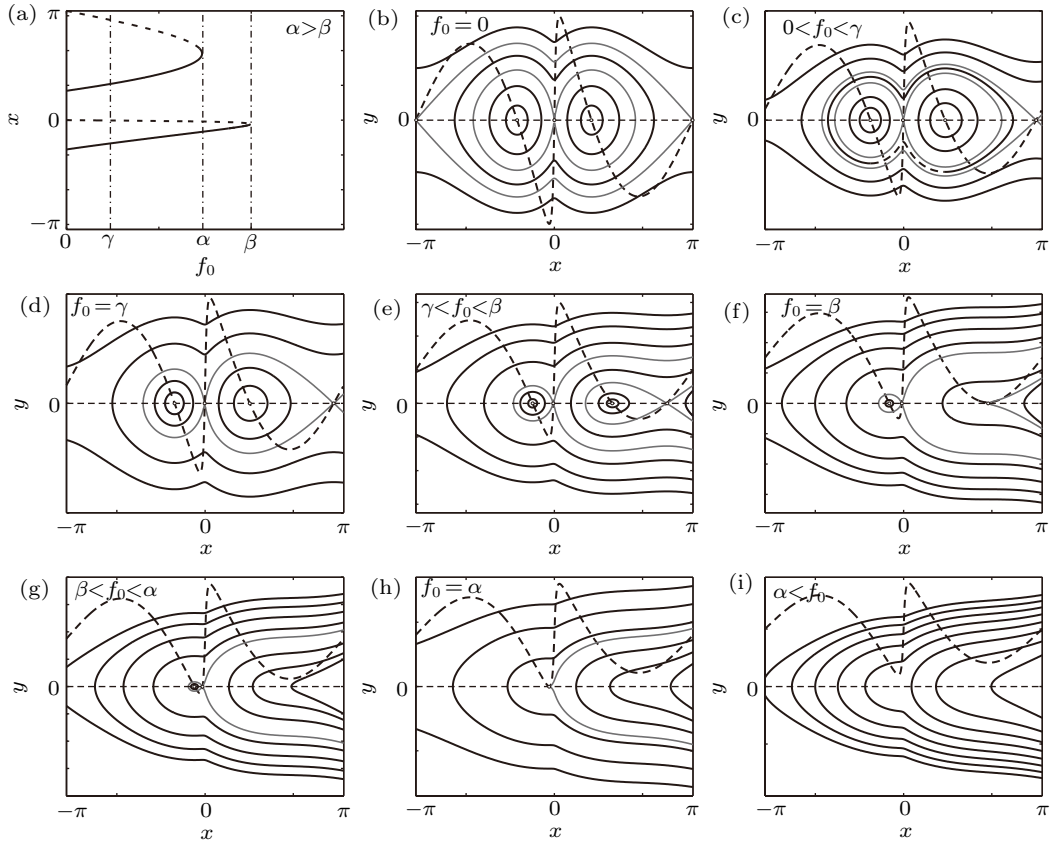


Fig. 8. Dynamic behavior of system (3) for $(\lambda,q)\in\mathrm{II}_2$: (a) the equilibrium bifurcation diagram for f_0 versus x, (b)–(i) the corresponding phase portraits and the nonlinear restoring forces marked by dashed lines.

With the help of the Hamiltonian function (11), when $(\lambda,q)\in\mathrm{II}$, the corresponding phase portraits are plotted for different values of parameter f_0 in Figs. 6–8, where the corresponding dashed lines represent the nonlinear restoring forces $F(x,f_0)$ for $\alpha<\beta$, $\alpha=\beta$ and $\alpha>\beta$, respectively. Take the phase portraits in Fig. 6 ($\alpha<\beta$) as an example, and the associated equilibrium bifurcation for f_0 versus x is depicted in Fig. 6(a): When $f_0=0$, the phase portraits of this pendulum system bear significant similarities to the coupling characteristics of the simple pendulum and the Duffing oscillator with a pair of Duffing-type homoclinic orbits and a pair of pendulum-type homoclinic orbits marked by the thick gray line, as shown in Fig. 6(b). As the constant excitation f_0 increases no more than γ, a pair of pendulum-type homoclinic orbits in Fig. 6(b) shrink into a large homoclinic orbit linking with one saddle point. Meanwhile, this large homoclinic orbit surrounds a pair

of asymmetric homoclinic orbits connecting the other saddle point, as shown in Fig. 6(c). When the constant excitation f_0 increases to γ, Fig. 6(d) shows that a pair of heteroclinic orbits connect one homoclinic orbit with a saddle point. It is worth pointing out that the large homoclinic orbit with two saddle points in Fig. 6(c) shrinks into a pair of heteroclinic orbits connecting one homoclinic orbit. For $\gamma < f_0 < \alpha$, the pair of heteroclinic orbits connecting one homoclinic orbit breaks and then bifurcates into two homoclinic orbits marked by thick gray line in Fig. 6(e). When the constant excitation f_0 continues to grow to α, one of the two homoclinic orbits shrinks into an equilibrium (sharp) depicted in Fig. 6(f). Increasing f_0 beyond β, Fig. 6(g) displays a homoclinic orbit connecting a saddle point. Then the homoclinic orbit shrinks into an equilibrium (sharp) for $f_0 = \beta$ in Fig. 6(h). Finally, the phase portrait without equilibrium is plotted for $f_0 > \beta$ in Fig. 6(i).

When $\alpha = \beta$, Fig. 7(a) shows the equilibrium bifurcation for f_0 versus x, which indicates that there exists four equilibria at $f_0 < \alpha$, two equilibria at $f_0 = \alpha$ and no equilibrium at $f_0 > \alpha$, respectively. Note that the phase portraits depicted in Figs. 7(b)–7(d) of this pendulum system bear significant similarities to those in Figs. 6(b)–6(d), respectively. Interestingly, two homoclinic orbits in Fig. 7(d) shrink synchronously into two equilibria (sharps) marked by green solid points for $f_0 = \alpha$ as seen in Fig. 7(e). Finally, the phase portrait without equilibrium is displayed for $f_0 > \alpha$ in Fig. 7(f). Similarly, the equilibrium bifurcation and the corresponding phase portraits in Figs. 8(b)–8(i) can be plotted and analyzed for $\alpha > \beta$, especially the transitions of homoclinic orbits, the equilibrium bifurcation and the corresponding nonlinear restoring forces.

4.2. The damping pendulum system with a small constant excitation

Under the sufficiently small perturbations of the viscous damping and constant excitation,[36,37] the limit cycle of this rotating pendulum will be analyzed by means of the Melnikov method in this subsection, especially the rotating limit cycle.

When $f_1 = 0$, we introduce the notation y for the velocity $\dot{x}$, the rotating pendulum system (2) becomes

$$\begin{aligned} \dot{x} &= y, \\ \dot{y} &= f_0 - \xi\dot{x} - \sin x \\ &\quad - q\lambda \sin x \left(1 - \frac{1}{\sqrt{1+\lambda^2 - 2\lambda\cos x}}\right), \end{aligned} \tag{12}$$

where parameters ξ and f_0 are sufficiently small. Note that system (12) is a typical dissipative system characterized by the strongly irrational nonlinearity. It is assumed that T_e represents a period of the periodic trajectories of system (3), the corresponding Melnikov function[38–40] of system (12) is given by

$$M(\xi, f_0) = \int_0^{T_e} [-\xi y(t) + f_0] y(t)\,\mathrm{d}t = -\xi I_1 + f_0 I_2, \tag{13}$$

where

$$I_1 = \int_0^{T_e} y^2(t)\,\mathrm{d}t, \quad I_2 = \int_0^{T_e} y(t)\,\mathrm{d}t. \tag{14}$$

The Melnikov function is proportional to the first variation of the distance function. Therefore, when the Melnikov function is zero, it predicts the intersection of stable and unstable manifolds. In other words, the limit cycle will be obtained and the system dynamics will be changed. The detailed classification of perturbed dynamics is shown in the following.

Case I When $e \in (E_n, E_0)$, two families of small closed orbits which encircle one equilibrium respectively are plotted in green in Fig. 3(b). Note that those orbits correspond to two small oscillatory motions on the left and right sides of this pendulum. There are a family of large closed orbits surrounding three equilibria for $e \in (E_0, E_p)$ that correspond to the large oscillatory motion of this pendulum, as shown in Figs. 3(a) and 3(b). Assuming T_e^o is the minimum positive period of the oscillatory motion denoted by $(x_e^o(t), y_e^o(t))$, and the corresponding Melnikov function of those closed orbits around the equilibrium is given by

$$M_o^e(\xi, f_0) = \int_0^{T_e^o} [-\xi y_e^o(t) + f_0] y_e^o(t)\,\mathrm{d}t = -\xi I_1^o + f_0 I_2^o, \tag{15}$$

where $I_1^o > 0$ and $I_2^o = 0$. It is found that, for ξ and f_0 sufficiently small, there is no value of e for which $M_o^e(\xi, f_0) = 0$, which indicates that there is no limit cycle around the equilibrium. Based upon Poincaré–Bendixson theory,[41] we can prove that there exists no limit cycle around the equilibrium in system (12). The associated phase portraits for $(\lambda, q) \in \mathrm{I}$ and II are shown in Figs. 9(a) and 10(a), respectively. For a better understanding of phase trajectories, the corresponding cylindrical phase portrait is plotted in Fig. 11(a).

Case II When $e = E_p$, the unperturbed system (3) presents a pair of pendulum-type homoclinic orbits whose solutions can be marked by $(x_{hom2}^{\pm}(t), y_{hom2}^{\pm}(t))$ as shown in Figs. 3(a) and 3(b). On the upper homoclinic orbit of pendulum-type $(x_{hom2}^{+}(t), y_{hom2}^{+}(t))$ satisfying $y_{hom2}^{+}(t) \geqslant 0$, we obtain the corresponding Melnikov function which depends on the two parameters ξ and f_0

$$\begin{aligned} M_{hom2}^{+}(\xi, f_0) &= -\xi \int_{-\infty}^{+\infty} \left(y_{hom2}^{+}(t)\right)^2 \mathrm{d}t + f_0 \int_{-\infty}^{+\infty} y_{hom2}^{+}(t)\,\mathrm{d}t \\ &= -\xi I_1^{hom2} + f_0 I_2^{hom2}, \end{aligned} \tag{16}$$

where $I_1^{hom2} > 0$ and $I_2^{hom2} = 2\pi$. On the lower pendulum-type homoclinic orbits $(x_{hom2}^{-}(t), y_{hom2}^{-}(t))$ satisfying $y_{hom2}^{-}(t) \leqslant 0$, the corresponding Melnikov function can be written as

$$\begin{aligned} M_{hom2}^{-}(\xi, f_0) &= -\xi \int_{-\infty}^{+\infty} \left(y_{hom2}^{-}(t)\right)^2 \mathrm{d}t + f_0 \int_{-\infty}^{+\infty} y_{hom2}^{-}(t)\,\mathrm{d}t \\ &= -\xi I_1^{hom2} + f_0 I_2^{hom2}, \end{aligned} \tag{17}$$

where $I_1^{hom2} > 0$ and $I_2^{hom2} = -2\pi$. The generalized integral value a_1 can be derived by using the numerical integration

$$a_1 = \int_{-\infty}^{+\infty} (y^{\pm}_{\text{hom2}}(t))^2 \mathrm{d}t = \int_{\mp\pi}^{\pm\pi} y^{\pm}_{\text{hom2}}(t)\,\mathrm{d}x$$
$$= 2\int_0^{\pi} \sqrt{2H(\pi,0) + 2(1+q\lambda)\cos x + 2q\sqrt{1+\lambda^2-2\lambda\cos x} - 4q\lambda + 2q - 2}\,\mathrm{d}x. \tag{18}$$

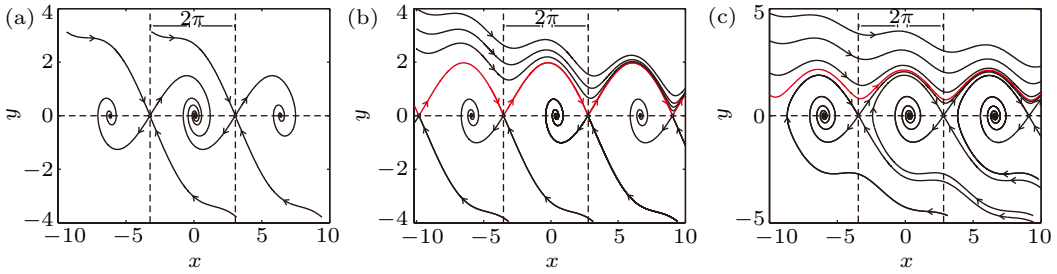


Fig. 9. Dynamic behaviors of the pendulum system with viscous damping and constant excitation for $(\lambda, q) \in$ I: (a) none of limit cycle surrounding the equilibrium for $2\pi f_0 - a_1\xi < 0$, (b) the bifurcation of the upper homoclinic orbit for $2\pi f_0 - a_1\xi = 0$, (c) a rotating limit cycle for $2\pi f_0 - a_1\xi > 0$.

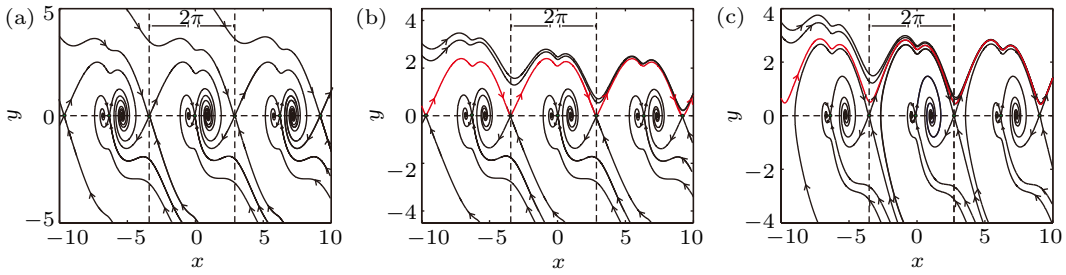


Fig. 10. Dynamic behaviors of the pendulum system with viscous damping and constant excitation for $(\lambda, q) \in$ II: (a) none of limit cycle surrounding the equilibrium for $2\pi f_0 - a_1\xi < 0$, (b) the bifurcation of upper homoclinic orbit for $2\pi f_0 - a_1\xi = 0$, (c) a rotating limit cycle for $2\pi f_0 - a_1\xi > 0$.

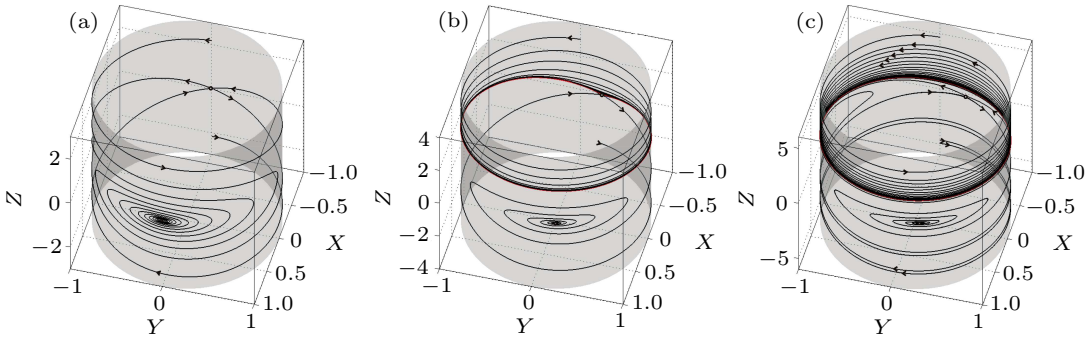


Fig. 11. Cylindrical phase portraits of the pendulum system with viscous damping and constant excitation for $q = 0, \xi = 0.2$ and $a_1 = 8$: (a) no limit cycle for $f_0 = 0.0001$, (b) the bifurcation of the upper homoclinic orbit for $f_0 \approx 0.2527$, (c) a rotating limit cycle for $f_0 = 0.3$.

According to the above Melnikov analysis, for the sufficiently small positive parameters ξ and f_0, we have a simple zero of $M^{+}_{\text{hom2}}(\xi, f_0) = 0$ at $2\pi f_0 - a_1\xi = 0$, which implies that the upper homoclinic orbit survives in a homoclinic bifurcation on a unique curve tangent to the line $2\pi f_0 - a_1\xi = 0$. There are no values of ξ and f_0 for $M^{-}_{\text{hom2}}(\xi, f_0) = 0$, so the lower homoclinic orbit is always broken.

When $e = E_0$, the similar computations can be carried out for the Duffing-type homoclinic orbits denoted by $(x^{\pm}_{\text{hom1}}(t), y^{\pm}_{\text{hom1}}(t))$ in Fig. 3(b). It is worth pointing out that the bifurcations of the Duffing-type homoclinic orbits must not exist due to $M_{\text{hom1}}(\xi, f_0) \neq 0$ for any parameters ξ and f_0. The associated phase portraits for $(\lambda, q) \in$ I and II are shown in Figs. 9(b) and 10(b), where the red trajectory connecting two saddle points corresponds to the bifurcation of the upper pendulum-type homoclinic orbit. In order to describe the homoclinic bifurcation, the corresponding cylindrical phase portrait is plotted in Fig. 11(b).

Case III When $e \in (E_{\text{p}}, +\infty)$, two families of symmetrical trajectories which correspond to rotary rather than oscillatory motions of this pendulum are plotted in Figs. 3(a) and 3(b). Assuming T^{r}_e is the minimum positive period of the rotary motion, we wish to compute values of parameters ξ and f_0 for which one (or both) of those orbits is (are) preserved. On the

upper trajectory $(x_e^+(t), y_e^+(t))$ satisfying $y_e^+(t) > 0$, we obtain the corresponding Melnikov function which depends on the two parameters ξ and f_0

$$\begin{aligned} M_{\rm r}^e(\xi, f_0) &= \int_0^{T_e^{\rm r}} \left[-\xi y_e^+(t) + f_0\right] y_e^+(t)\,{\rm d}t \\ &= -\xi I_1^{\rm r} + f_0 I_2^{\rm r}, \end{aligned} \tag{19}$$

where $I_1^{\rm r} > 0$ and $I_2^{\rm r} = 2\pi$. We conclude that, for the fixed parameters ξ and f_0 sufficiently small, there is precisely one value of $e = e^*$ for which $M_{\rm r}^e(\xi, f_0) = 0$, and that $M_{\rm r}^e(\xi, f_0) < 0$ ($M_{\rm r}^e(\xi, f_0) > 0$) for $e > e^*$ ($e < e^*$). It follows that there is a unique attracting closed orbit (rotating limit cycle) encircling the phase cylinder, the detailed proof of uniqueness of the attracting rotating limit cycle as seen in Ref. [42]. Note that e^* increases as f_0/ξ increases.

On the lower trajectory $(x_e^-(t), y_e^-(t))$ satisfying $y_e^-(t) < 0$, the corresponding Melnikov function which depends on the two parameters ξ and f_0 can be written as

$$\begin{aligned} M_{\rm r}^e(\xi, f_0) &= \int_0^{T_e^{\rm r}} \left[-\xi y_e^-(t) + f_0\right] y_e^-(t)\,{\rm d}t \\ &= -\xi I_1^{\rm r} + f_0 I_2^{\rm r}, \end{aligned} \tag{20}$$

where $I_1^{\rm r} > 0$ and $I_2^{\rm r} = -2\pi$. For the fixed parameters ξ and f_0 sufficiently small, there is no value of h for which $M_{\rm r}^e(\xi, f_0) = 0$, which indicates that the rotating limit cycle does not exist for $y_e^-(t) < 0$. The associated phase portraits for $(\lambda, q) \in$ I and II are shown in Figs. 9(c) and 10(c), respectively. In order to describe the rotating limit cycle, the corresponding cylindrical phase portrait is plotted in Fig. 11(c). Note that the equilibria with green solid points depicted in Figs. 9–11 correspond to the unstable saddle points or stable focuses.

4.3. Chaotic dynamics of the pendulum system with multiple excitations

In order to further demonstrate the complex dynamic behavior of the rotating pendulum system subjected to the sufficiently small perturbations of the viscous damping, constant force and periodic excitation,[43] the Melnikov method is employed to detect chaos in the sense of Smale's horseshoes caused by the transversal intersection of homoclinic orbits[38–40] in this subsection.

The corresponding Melnikov function for the homoclinic orbits of Duffing-type $(y_{\rm hom1}^{\pm}(t))$ is given by

$$\begin{aligned} &M_{\rm hom1}^{\pm}(\tau) \\ &= \int_{-\infty}^{+\infty} \left[-\xi y_{\rm hom1}^{\pm}(t) + f_0 + f_1\cos\omega(t+\tau)\right] y_{\rm hom1}^{\pm}(t)\,{\rm d}t \\ &= -\xi I_1^{\rm hom1} + f_0 I_2^{\rm hom1} - f_1\sin(\omega\tau) I_3^{\rm hom1}, \end{aligned} \tag{21}$$

where

$$\begin{aligned} I_1^{\rm hom1} &= \int_{-\infty}^{+\infty} \left(y_{\rm hom1}^{\pm}(t)\right)^2 {\rm d}t, \\ I_2^{\rm hom1} &= \int_{-\infty}^{+\infty} y_{\rm hom1}^{\pm}(t)\,{\rm d}t = 0, \\ I_3^{\rm hom1} &= \int_{-\infty}^{+\infty} y_{\rm hom1}^{\pm}(t)\sin(\omega t)\,{\rm d}t. \end{aligned} \tag{22}$$

We define $M_{\rm hom1}^{\pm}(\tau) = 0$, yielding

$$\begin{aligned} R_{\rm hom1}^{\pm}(\omega) &= \left|\frac{\xi I_1^{\rm hom1} - f_0 I_2^{\rm hom1}}{f_1 I_3^{\rm hom1}}\right| = \left|\frac{I_1^{\rm hom1} - \sigma\, I_2^{\rm hom1}}{\mu\ I_3^{\rm hom1}}\right| \\ &= \frac{1}{\mu}\left|\frac{I_1^{\rm hom1}}{I_3^{\rm hom1}}\right| = |\sin(\omega\tau)|, \quad \sigma = \frac{f_0}{\xi},\ \mu = \frac{f_1}{\xi}. \end{aligned} \tag{23}$$

Similar computations can be carried out for the homoclinic orbits of pendulum-type $(y_{\rm hom2}^{\pm}(t))$, and the corresponding Melnikov function of the orbits is given by

$$\begin{aligned} &M_{\rm hom2}^{\pm}(\tau) \\ &= \int_{-\infty}^{+\infty} \left[-\xi y_{\rm hom2}^{\pm}(t) + f_0 + f_1\cos\omega(t+\tau)\right] y_{\rm hom2}^{\pm}(t)\,{\rm d}t \\ &= -\xi I_1^{\rm hom2} + f_0 I_2^{\rm hom2} + f_1\cos(\omega\tau) I_3^{\rm hom2}, \end{aligned} \tag{24}$$

where

$$\begin{aligned} I_1^{\rm hom2} &= \int_{-\infty}^{+\infty} \left(y_{\rm hom2}^{\pm}(t)\right)^2 {\rm d}t, \\ I_2^{\rm hom2} &= \int_{-\infty}^{+\infty} y_{\rm hom2}^{\pm}(t)\,{\rm d}t = \pm 2\pi, \\ I_3^{\rm hom2} &= \int_{-\infty}^{+\infty} y_{\rm hom2}^{\pm}(t)\cos(\omega t)\,{\rm d}t. \end{aligned} \tag{25}$$

When $M_{\rm hom1}^{\pm}(\tau) = 0$, we have

$$\begin{aligned} R_{\rm hom2}^{\pm}(\omega) &= \left|\frac{\xi I_1^{\rm hom2} - f_0 I_2^{\rm hom2}}{f_1 I_3^{\rm hom2}}\right| = \left|\frac{I_1^{\rm hom2} - \sigma I_2^{\rm hom2}}{\mu\ I_3^{\rm hom2}}\right| \\ &= |\cos(\omega\tau)|, \quad \sigma = \frac{f_0}{\xi},\ \mu = \frac{f_1}{\xi}. \end{aligned} \tag{26}$$

In order to detect the chaotic boundary of the pendulum system (2), we introduce the following function:

$$\overline{R}_{\rm hom}(\omega) = {\rm Min}\left\{R_{\rm hom1}^{+}(\omega),\ R_{\rm hom1}^{-}(\omega),\ R_{\rm hom2}^{+}(\omega),\ R_{\rm hom2}^{-}(\omega)\right\}, \tag{27}$$

where $R_{\rm hom1}^{+}(\omega) = R_{\rm hom1}^{-}(\omega)$ and $R_{\rm hom2}^{+}(\omega) < R_{\rm hom2}^{-}(\omega)$. For all parameters satisfying $\overline{R}_{\rm hom}(\omega) > 1$, the chaotic motion of the rotating pendulum system (2) is practically nonexistent. Once the chaos in the sense of Smale's horseshoes caused by the transversal intersection of homoclinic orbits occurs, all parameters must satisfy $\overline{R}_{\rm hom}(\omega) < 1$. Notice that $\overline{R}_{\rm hom}(\omega) < 1$ is a necessary condition rather than a sufficient condition for chaos to exist.

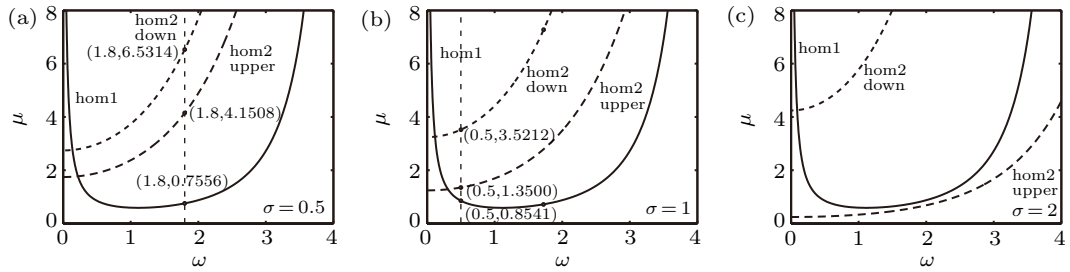


Fig. 12. The chaotic boundaries detected by the Melnikov analysis for the Duffing-type and pendulum-type homoclinic orbits at $q = 3$ and $\lambda = 1.5$: (a) $\sigma = 0.5$ ($R^{\pm}_{\rm hom1}(1.8) = 0.7556$, $R^{+}_{\rm hom2}(1.8) = 4.1508$, $R^{-}_{\rm hom2}(1.8) = 6.5314$), (b) $\sigma = 1$ ($R^{\pm}_{\rm hom1}(0.5) = 0.8541$, $R^{+}_{\rm hom2}(0.5) = 1.3500$, $R^{-}_{\rm hom2}(0.5) = 3.5212$), (c) $\sigma = 2$.

When $q = 3$ and $\lambda = 1.5$, the chaotic boundary graphs with three different structures are plotted using the above Melnikov analysis for different value of parameter $\sigma = 0.5, 1$ and 2. The detailed description can be seen in Figs. 12(a)–12(c), respectively, where one boundary denoted by the solid curve corresponds to the Duffing-type homoclinic orbits for $R^{\pm}_{\rm hom1}(\omega) = 1$, the dashed curve represents the upper pendulum-type homoclinic orbit for $R^{+}_{\rm hom2}(\omega) = 1$ and the remaining dotted curve is the chaotic boundary of the lower pendulum-type homoclinic orbit for $R^{-}_{\rm hom2}(\omega) = 1$.

Numerical simulations, including the bifurcation diagram, phase portrait, time history[44] and Poincaré section,[45] are carried out to verify the efficiency of the criteria derived by the Melnikov analysis in the following. Figure 13(a) shows the bifurcation diagram of the external harmonic forcing f_1 versus angular displacement x with three detected criteria $f_1^{\rm hom1} = 0.0453$, $f_1^{\rm hom2^+} = 0.2490$ and $f_1^{\rm hom2^-} = 0.3919$ for parameters $q = 3$, $\lambda = 1.5$, $\xi = 0.06$, $f_0 = 0.03$, $\omega = 1.8$ fixed. The bifurcation diagrams are plotted from different initial conditions $(x, y) = (1, 0)$ and $(-1, 0)$ marked by black and gray, respectively, from which multiple periodic windows and chaotic regions can be seen. The corresponding Lyapunov exponents can be plotted in Fig. 13(b) under the initial condition $(x, y) = (-1, 0)$. It is obvious from Fig. 13(a) that no chaotic motion is observed below the chaotic boundary $f_1 = 0.0453$ marked by the solid line. The predicted chaotic boundary can be derived by letting $\overline{R}_{\rm hom}(1.8) = 1$. Then, we analyze the complex system which has the properties of essential nonlinearity in terms of periodic solution and chaotic solution. When f_1 increases beyond the threshold value 0.0453 reaching around 0.33, the system jumps to the chaotic motion from a pair of period-1 solutions whose phase portraits and time histories are plotted for $f_1 = 0.1$ in Figs. 13(c) and 13(d). Enlarging the parameter f_1 to 0.65, the proposed system exhibits a period-3 motion of which phase portrait is displayed in Fig. 13(e) and the corresponding time history $x(t)$ is shown in Fig. 13(f). Additionally, for $f_1 = 1.5$, a high periodic solution is presented in Fig. 13(g) and the corresponding time history $x(t)$ can be shown in Fig. 13(h). With the help of the time history $x(t)$, a single complete cycle of such periodic motion is given in Figs. 13(d), 13(f), and 13(h), which allows ones to understand the law of complex periodic motion in detail. Interestingly, the evolution law of the chaotic attractors can be described by increasing parameter f_1, as shown in Figs. 13(i)–13(k), respectively. Interestingly, the structure of chaotic attractor depicted in Fig. 13(i) bears significant similarities to the SD attractor, which indicates that the system mainly reflects the oscillating characteristics, as seen in Ref. [31]. Note that the chaotic attractor depicted in Fig. 13(k) is similar to the coupling of the pendulum attractor and the SD attractor, which reflects the mixing of oscillating and rotating motions.

Similarly, the bifurcation diagram of the external harmonic forcing f_1 versus angular displacement x with three detected criteria $f_1^{\rm hom1} = 0.0427$, $f_1^{\rm hom2^+} = 0.0675$ and $f_1^{\rm hom2^-} = 0.1761$ is displayed for parameters $q = 3$, $\lambda = 1.5$, $\xi = 0.05$, $f_0 = 0.05$, $\omega = 0.5$, as shown in Fig. 14(a). Note that the bifurcation diagram is plotted from the initial condition $(x, y) = (1, 0)$. It is clear from the bifurcation diagram that no chaotic motion is observed below the chaotic boundary $f_1 = 0.0427$ ($\overline{R}_{\rm hom}(0.5) = 1$) predicted by the Melnikov method and marked by the solid line. For a better understanding of periodic windows and chaotic regions, a local enlargement of the bifurcation diagram can be presented for $f_1 \in [1.5, 1.8]$ in Fig. 14(b). It is found that there exist some tiny periodic windows in Fig. 14(b). Due to the coupling nonlinearities of the simple pendulum and the Duffing oscillator,[34,37] for $f_1 = 0.8$, the chaotic attractor depicted in Fig. 14(c) bears significant similarities to the Duffing attractor,[46] which means that the system mainly reflects the oscillating characteristics. The time history of oscillating chaotic motion satisfying $|x(t)| < \pi$ for any time can be seen in Fig. 14(f). Clearly, the chaotic attractor for $f_1 = 1.55$ depicted in Fig. 14(d) is similar to the coupling of the pendulum attractor and the Duffing attractor, which reflects the mixing of oscillating and rotating motions. The corresponding time history $x(t)$ is shown in Fig. 14(g), and the law of chaotic motions are marked including oscillation and rotation respectively. When $f_1 = 1.8$, the chaotic attractor depicted in Fig. 14(e) is similar to the pendulum attractor, which mainly reflects the rotating motions. The corresponding time history $x(t)$ is shown in Fig. 14(h), and the law of chaotic motions are marked including oscillation and rotation respectively. The corresponding large Lyapunov ex-

ponents (LE) can be marked in Figs. 14(d)–13(f). To demonstrate the motions of the tiny periodic windows in Fig. 14(b), three stable periodic trajectories are displayed after long irregular movement in Figs. 14(i)–14(k), respectively. Compared to the standard periodic motion, the three travelable periodic motions[47] are asymmetric and no centers for periodic motions exist. In other words, the periodic motion in pendulum possesses both rotations and oscillations.

It is worth pointing out that the boundary $\overline{R}_{\rm hom}(\omega) = 1$ is a necessary condition for chaos to exist rather than a sufficient condition.[48] In order to further verify the rationality of the chaotic region derived by the Melnikov analysis, a two-dimensional parameter space plot in the range of $f_0 \in [0,2]$ and $\omega \in [1,4]$ is displayed for $q = 3$, $\lambda = 1.5$, $\xi = 0.2$,[39,48,49] as seen in Fig. 15(a). The gray region, which can be obtained by calculating the largest Lyapunov exponents, corresponds to chaotic motion with positive Lyapunov exponent.

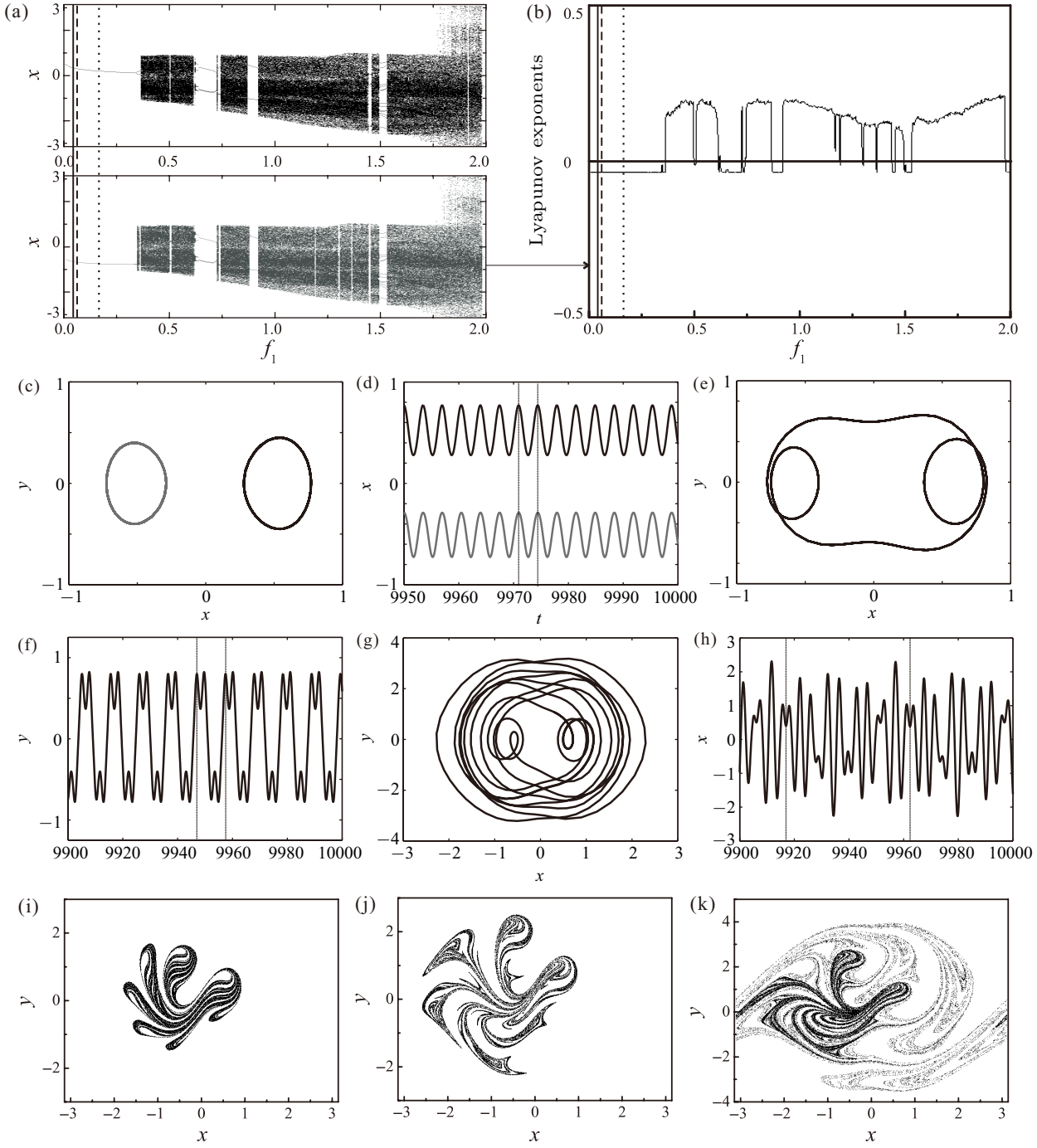


Fig. 13. When $q = 3$, $\lambda = 1.5$, $\xi = 0.06$, $f_0 = 0.03$ and $\omega = 1.8$: (a) bifurcation diagram for f_1 versus x with the threshold values $f_1^{\rm hom1} = 0.0427$ (solid line), $f_1^{\rm hom2^+} = 0.0675$ (dashed line) and $f_1^{\rm hom2^-} = 0.1761$ (dotted line), (b) the corresponding largest Lyapunov exponents under the initial condition $(1,0)$; (c) the phase portraits of a pair of period-1 solutions for $f_1 = 0.1$ and their time histories (d); (e) the phase portrait of period-3 solution for $f_1 = 0.65$ and the corresponding time history (f); (g) the phase portrait of period-13 solution for $f_1 = 1.5$ and the corresponding time history (h); (i)–(k) three chaotic attractors for $f_1 = 0.92$, 1.7, 1.9, respectively.

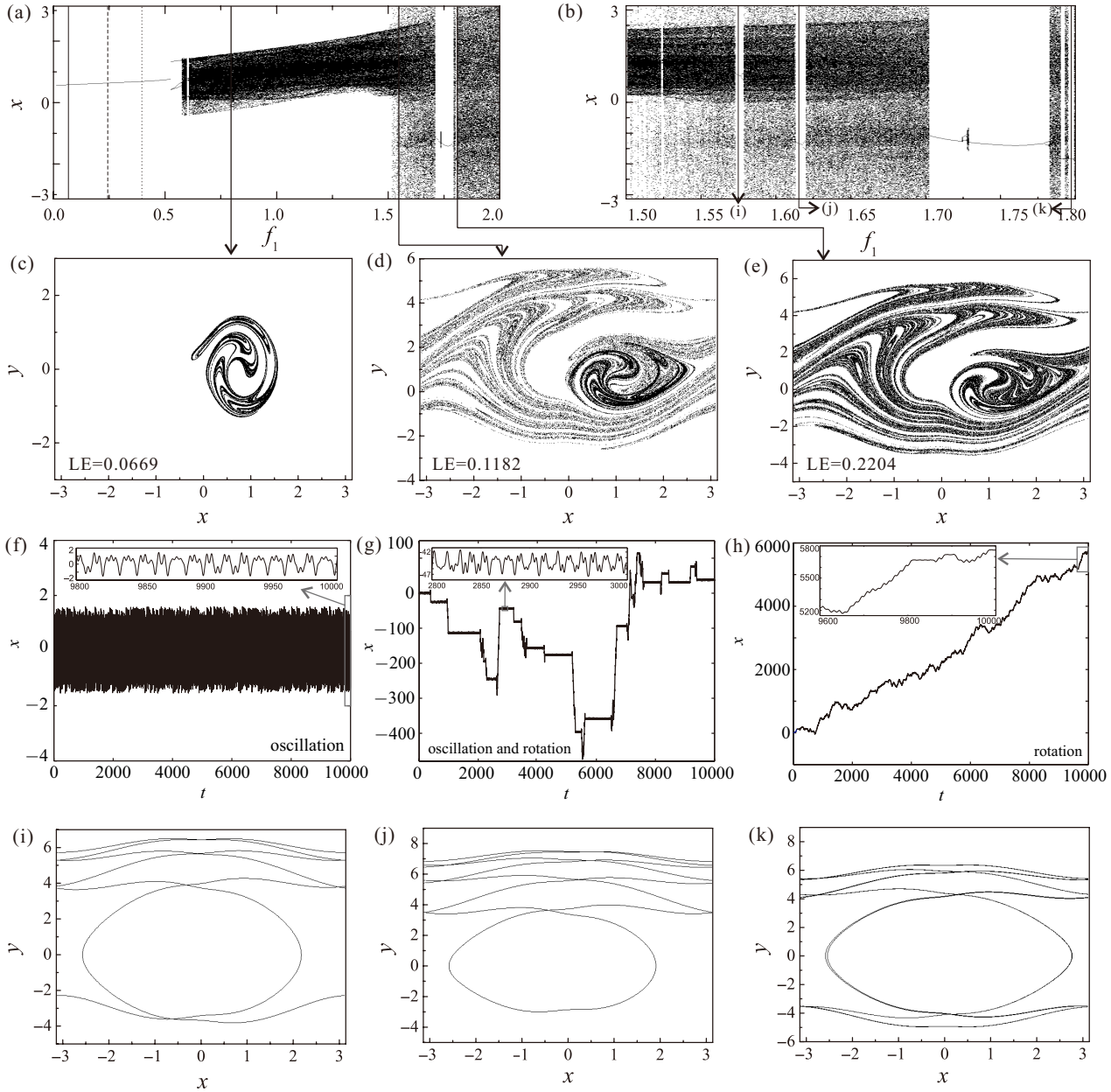


Fig. 14. When $q=3$, $\lambda=1.5$, $\xi=0.05$, $f_0=0.05$ and $\omega=0.5$: (a) bifurcation diagram for f_1 versus x with the threshold values $f_1^{\rm hom1}=0.0453$ (solid line), $f_1^{\rm hom2^+}=0.2490$ (dashed line) and $f_1^{\rm hom2^-}=0.3919$ (dotted line); (b) the local enlargements for $f_1\in[1.5,1.8]$; (c)–(e) three types of chaotic motions for $f_1=0.8$, 1.55, 1.8 and the corresponding time histories (f)–(h); (i)–(k) three periodic motions for $f_1=1.575$, 1.616, 1.78, respectively.

Furthermore, the theoretical threshold of the chaotic region marked by the black curve in Fig. 15(a) can be displayed by letting $\overline{R}_{\rm hom}(\omega)=1$. It is concluded that the gray region shows a good agreement with the theoretical analysis satisfying $\overline{R}_{\rm hom}(\omega)>1$. For a better understanding of the theoretical chaotic threshold, we take $\omega=1.515$ as an example. Figure 15(b) shows the bifurcation diagrams for f_1 versus x with the predicted criteria $f_1=0.13$ marked by the solid line. The corresponding Lyapunov exponents is plotted in Fig. 15(c). It is found from Figs. 15(b) and 15(c) that the predicted chaotic threshold is close to the real chaotic threshold.

In order to demonstrate the classification of oscillation and rotation in chaotic motions, we introduce the cylindrical phase portraits in Fig. 16. The oscillating chaotic motions, of which the chaotic attractors depicted in Figs. 13(g) and 14(d), bear significant similarities to the SD attractor and the Duffing attractor, respectively, and can be displayed in Figs. 16(a) and 16(b). As is clearly seen in Fig. 16(c), the cylindrical phase portraits for the chaotic motion of rotation coupled with oscillation are illustrated, which indicates that the pendulum shows both the irregular reciprocating movement in the neighborhood of the equilibrium and the irregular rotating movement around the point A depicted in Fig. 1. Obviously, Fig. 16(d) shows the cylindrical phase portrait for the chaotic motion of the oscillation coupled with rotation, which mainly reflects the irregular rotating motion due to the majority of trajectories surrounding the cylinder.

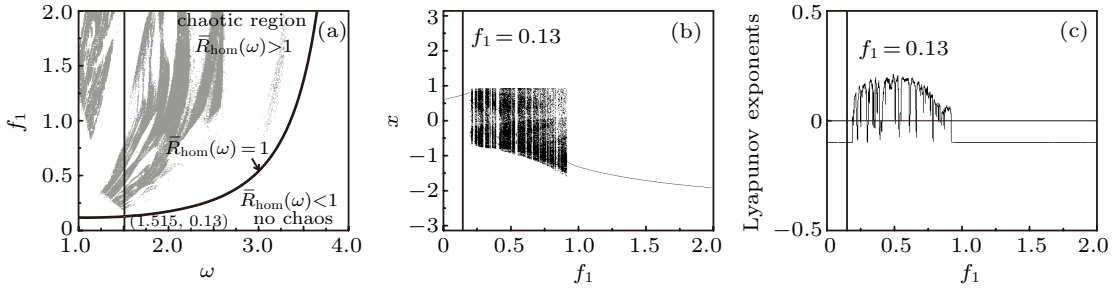


Fig. 15. (a) A two-dimensional parameter space plot for $q=3$, $\lambda=1.5$, $f_0=0.1$, $\xi=0.2$ in the range of $f_1\in[0,2]$ and $\omega\in[1,4]$ and theoretical boundary derived by the Melnikov analysis, (b) the bifurcation diagram of f_1 with the threshold $f_1=0.13$ and (c) the corresponding Lyapunov exponents for $\xi=1.515$ (the gray region corresponds to the chaotic region, the white region represents non-chaotic region and the black curve $\bar{R}_{\rm hom}(\omega)=1$ is the theoretical boundary of chaos).

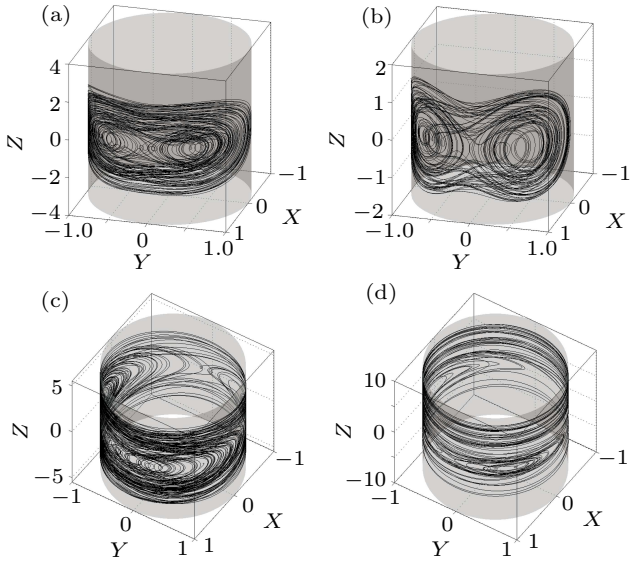


Fig. 16. Cylindrical phase portraits of oscillations starting initial condition $(x,y)=(1,0)$: (a) SD-type chaotic motion, (b) Duffing-type chaotic motion; chaotic cylindrical phase portraits of the coupling of oscillations and rotations (c) and (d).

5. Conclusions

In this paper, we have theoretically and numerically investigated the dynamic behavior of a classical rotating pendulum system with viscous damping, constant and periodic excitations using nonlinear dynamical techniques. This complex pendulum system exhibits strongly intrinsic nonlinearity due to its nonlinear restoring force with the coupling of the irrational term, the fractional term and the trigonometric function. The salient features of the unperturbed pendulum system bear significant similarities to the coupling characteristics of a simple pendulum and a Duffing oscillator with coexistence of the Duffing-type and pendulum-type homoclinic orbits. The results are as follows:

(i) Based upon the Hamiltonian with a large constant excitation, all types of phase portraits are classified and analyzed over a period $x\in[-\pi,\pi]$ especially the transitions of singular closed orbits, which is in favor of understanding the effect of the constant force on a simple rotating machinery system.

(ii) Under the sufficiently small perturbations of the viscous damping and constant excitation, the dissipative pendulum system exhibits a range of interesting nonlinear phenomena, such as the bifurcation of the upper pendulum-type homoclinic orbit and the rotating limit cycle. Particularly, it is found that there exists a unique attracting rotating limit cycle unlike the standard limit cycle around the equilibrium.

(iii) The Melnikov method is employed to detect the chaotic thresholds of the rotating pendulum system subjected to the sufficiently small values of viscous damping, constant and periodic excitations. According to the theoretical analysis, we derive three chaotic boundaries which correspond to the Duffing-type homoclinic orbits, the upper and lower pendulum-type homoclinic orbits, respectively, due to the effect of constant excitation. Finally, the numerical simulations show a brief description of global behavior including multiple periodic motions and different types of chaotic motions by means of bifurcation diagram, Poincaré section, time history and cylindrical phase portrait.

References

[1] Peters R D 2004 *Sci. Educ.* **13** 279
[2] Matthews M R, Gauld C F and Stinner A 2005 *The Pendulum: Scientific, Historical, Philosophical and Educational Perspectives* (Dordrecht: Springer) p. 139
[3] Parks H V and Faller J E 2010 *Phys. Rev. Lett.* **105** 110801
[4] Carroll S P, Owen J S and Hussein M F M 2014 *J. Sound Vib.* **333** 5865
[5] Stachowiak T and Okada T 2006 *Chaos Solitons Fract.* **29** 417
[6] Roy J, Mallik A K and Bhattacharjee J K 2013 *Nonlinear Dyn.* **73** 993
[7] Eissa M and Sayed M 2008 *Commun. Nonlinear Sci. Numer. Simul.* **13** 465
[8] Gitterman M 2010 *Physica A* **389** 3101
[9] Paula A S D, Savi M A, Wiercigroch M and Pavlovskaia E 2012 *Int. J. Bifur. Chaos* **22** 1250111
[10] Horton B, Wiercigroch M and Xu X 2008 *Philos. Trans. R. Soc. A* **366** 767
[11] Bartuccelli M V, Gentile G and Georgiou K V 2001 *Proc. R. Soc. London A* **457** 3007
[12] Han N and Cao Q J 2016 *Int. J. Non-Linear Mech.* **88** 122
[13] Xu X and Wiercigroch M. 2007 *Nonlinear Dyn.* **47** 311
[14] Das S and Wahi P 2016 *Proc. R. Soc. A* **472** 20160719
[15] Zhang H and Ma T W 2012 *Nonlinear Dyn.* **70** 2433
[16] Koch B P and Leven R W 1985 *Physica D* **16** 1
[17] Ji J C and Chen Y S 1999 *Appl. Math. Mech.* **20** 350
[18] Albert Luo C J and Min F H 2011 *Commun. Nonlinear Sci. Numer. Simulat.* **16** 4704
[19] Leven R W and Koch B P 1981 *Phys. Lett. A* **86** 71
[20] Kapitaniak M, Czolczynski K, Perlikowski P and Kapitaniak T 2012 *Phys. Rep.* **517** 1
[21] Najdecka A, Kapitaniak T and Wiercigroch M. 2015 *Int. J. Non-Linear Mech.* **70** 84

[22] Wojna M, Wijata A, Wasilewski G and Awrejcewicz J. 2018 *J. Sound Vib.* **430** 214
[23] Alevras P, Brown I and Yurchenko D. 2015 *Nonlinear Dyn.* **81** 201
[24] Wu S T and Siao P S 2012 *J. Sound Vib.* **331** 3020
[25] Mahmoudkhani S 2018 *J. Sound Vib.* **425** 102
[26] Najdecka A, Narayanan S and Wiercigroch M 2015 *Int. J. Non-Linear Mech.* **71** 30
[27] Jia M M, Jiang H G, Li W J 2019 *Acta Phys. Sin.* **68** 130503 (in Chinese)
[28] Cao Q J, Han N and Tian R L 2011 *Chin. Phys. Lett.* **28** 0605021
[29] Han N, Cao Q J and Wiercigroch M 2013 *Int. J. Bifur. Chaos* **23** 1350074
[30] Han N and Cao Q J 2016 *Commun. Nonlinear Sci. Numer. Simulat.* **36** 431
[31] Cao Q J, Wiercigroch M, Pavlovskaia E E, Grebogi C and Thompson J M T 2006 *Phys. Rev. E* **74** 046218
[32] Li Z X, Cao Q J and Alain L 2016 *Chin. Phys. B* **25** 010502
[33] Hong L and Xu J 2004 *Commun. Nonlinear Sci. Numer. Simulat.* **9** 313
[34] Ueda Y 2006 *Ann. New York Acad. Sci.* **357** 422
[35] Zhang X H and Zhou L Q 2018 *Appl. Math. Model.* **61** 744
[36] Hou L, Chen H Z, Chen Y S, Lu K and Liu Z S 2019 *Mech. Syst. Signal Process.* **125** 65
[37] Hou L, Su X C and Chen Y S 2019 *Int. J. Bifur. Chaos* **29** 1950173
[38] Cao Q J, Wiercigroch M, Pavlovskaia E E, Grebogi C and Thompson J M T 2008 *Philos. Trans. R. Soc. A* **366** 635
[39] Guckenheimer J and Holmes P 1983 *Nonlinear Oscillations, Dynamical Systems, and Bifurcations of Vector Fields* (New York: Springer) p. 184
[40] Melnikov V K 1963 *Trans. Moscow. Math. Soc.* **12** 1
[41] Hu H Y 2000 *Applied Nonlinear Dynamics* (Beijing: Aviation Industry Press of China) p. 38 (in Chinese)
[42] Strogatz S H 2015 *Nonlinear Dynamics and Chaos: With Applications to Physics, Biology, Chemistry, and Engineering* (Beijing: China Machine Press) p. 272
[43] Kwekt K H and Li J B 1996 *Int. J. Non-Linear Mech.* **31** 277
[44] Sun J C 2016 *Chin. Phys. Lett.* **33** 100503
[45] Gao F, Li W Q, Tong H Q *et al.* 2019 *Chin. Phys. B* **28** 090501
[46] Seydel R 1985 *Physica D* **17** 308
[47] Albert Luo C J 2017 *Resonance and Bifurcation to Chaos in Pendulum* (Beijing: Higher Education Press of China) p. 220
[48] Liu Y Z and Chen L Q 2001 *Nonlinear Vibrations* (Beijing: Aviation Industry Press of China) p. 286 (in Chinese)
[49] Feng J Q 2018 *Nonlinear Dynamics of a Typical Vibro-Impact System* (Beijing: Science Press of China) p. 95 (in Chinese)